Electrochimica Acta 404 (2022) 139620

Contents lists available at ScienceDirect

Electrochimica Acta

journal homepage: www.elsevier.com/locate/electacta

Dual redox groups enable organic cathode material with a high capacity for aqueous zinc-organic batteries

Yongkang An[a], Yu Liu[a], Shuangshuang Tan[a], Fangyu Xiong[a], Xiaobin Liao[b], Qinyou An[a,c,*]

[a] State Key Laboratory of Advanced Technology for Materials Synthesis and Processing, Wuhan University of Technology, Wuhan, Hubei 430070, China
[b] State Key Laboratory of Silicate Materials for Architectures, International School of Materials Science and Engineering, Wuhan University of Technology, Wuhan 430070, China
[c] Foshan Xianhu Laboratory of the Advanced Energy Science and Technology, Guangdong Laboratory Xianhu Hydrogen Valley, Foshan, Guangdong 528200, China

ARTICLE INFO

Article history:
Received 20 September 2021
Revised 6 November 2021
Accepted 17 November 2021
Available online 20 November 2021

Keywords:
Aqueous Zn-organic batteries
Organic electrodes
Carbonyls
Pyrazines
High capacity

ABSTRACT

Organic cathode materials have recently attracted extensive attention in aqueous zinc-organic batteries (ZOBs) due to their safety, abundant resources, and designability. However, the most as-reported organic materials with a single redox site exhibit limited specific capacities. Herein, benzo [i] benzo [6,7] quinoxalino [2, 3-a] benzo [6,7] quinoxalino [2, 3-c] phenazine-5, 8, 13, 16, 21, 24-hexaone (TBQPH) with both carbonyls and pyrazines as redox groups is designed and synthesized as ZOBs cathode material. The dual redox sites in TBQPH enable a high specific capacity of 455.8 mAh g^{-1} at 0.3 A g^{-1} owing to the 12-electron reaction mechanism. *Ex-situ* spectroscopic techniques (especially liquid NMR spectrum) and density functional theory calculations provide strong evidence for the insertion/extraction of hydrogen ions. More importantly, the TBQPH electrode exhibits an ultra-long cycle life of 10,000 cycles at 10 A g^{-1} with an average decay of only 0.0022% per cycle, which is attributed to the fast reaction kinetics and low charge transfer resistance. This work inspires new inspiration for designing next-generation high-performance organic electrode materials.

1. Introduction

Lithium-ion batteries (LIBs) possess the advantages of stable cycle life and high energy density. [1–4] However, limited resources and high cost restrict their further applications [5–7]. Aqueous zinc ion batteries (ZIBs) feature high theoretical capacity (820 mAh g^{-1}), abundant resources, suitable redox potential (−0.762 V vs. the standard hydrogen electrode (SHE)), and environmental friendliness, have been aroused widespread attention as a promising energy storage system [8–11]. Generally, the cathode materials play a decisive role in the electrochemical performance of ZIBs. Inspired by the conventional LIBs, a large number of inorganic cathode materials have been developed, such as Prussian blue analogs [12,13], vanadium-based materials [14,15], and manganese-based materials [16,17]. However, owing to the intercalation of hydrated Zn^{2+} and H^+ leading to volume expansion and the destruction of crystal lattices [17–19], these inorganic substances usually exhibit poor cycling stability. Therefore, it is urgent to develop novel cathode materials to make up for this situation.

Organic electrode materials have been widely applied in alkali metal ion (e.g. Li^+ and Na^+) batteries because they can participate in energy storage through reversible coordination reactions [20–24]. Organic materials as electrodes have been displayed numerous attractive properties, such as abundant resources, designability, inexpensiveness, and long cycle life [25–28]. Moreover, such coordination reactions had also been proven to store multivalent ions [29–33]. For example, Wang et al. reported a sulfur heterocyclic quinone dibenzo[*b,i*]thianthrene-5,7,12,14-tetraone (DTT) molecule with carbonyl groups as cathode materials for Zn-organic batteries (ZOBs), and a reversible capacity (210.9 mAh g^{-1} at 50 mA g^{-1}) was realized [34]. Niu et al. reported a diquinoxalino[2,3-a: 2′,3′-c] phenazine (HATN) molecule with pyrazine groups for aqueous ZOBs [35]. The ultra-long cycle performance of the batteries was achieved through the uptake/removal behavior of hydrogen ions on the highly reversible C=N bond. Organic materials with C=O or C=N groups as a single redox group have been widely reported but exhibited a limited specific capacity for ZOBs [36–39]. The coexistence of two or more redox groups provides greater flexibility in the design of electrode materials and may achieve a higher theoretical capacity. However, the design of high-capability organic

* Corresponding author at: State Key Laboratory of Advanced Technology for Materials Synthesis and Processing, Wuhan University of Technology, Wuhan, Hubei 430070, China.
E-mail address: anqinyou86@whut.edu.cn (Q. An).

https://doi.org/10.1016/j.electacta.2021.139620
0013-4686/

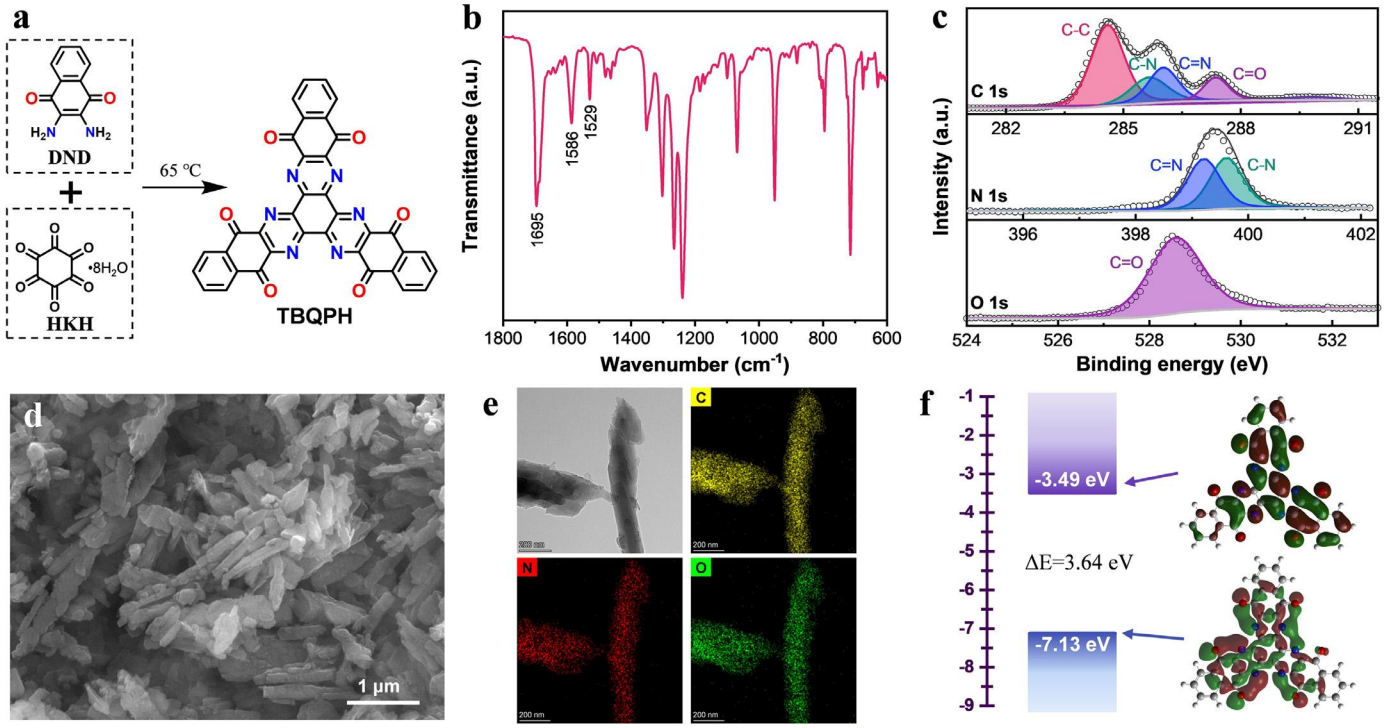

Fig. 1. (a) Synthesis route of TBQPH. (b) FT-IR spectrum of TBQPH. (c) High resolution C 1 s, N 1 s and O 1 s XPS spectra of TBQPH. SEM image (d) and TEM-EDS mappings (e) of TBQPH. (f) HOMO/LUMO energy levels of TBQPH (For interpretation of the references to color in this figure, the reader is referred to the web version of this article.).

molecules with dual redox groups still faces many difficulties, such as complicated synthesis processes, reduction in the proportion of redox groups, and solubility. Furthermore, the corresponding storage mechanisms also need to be explored in deep.

In this work, benzo [i] benzo [6, 7] quinoxalino [2, 3-a] benzo [6, 7] quinoxalino [2, 3-c] phenazine-5, 8, 13, 16, 21, 24-hexaone (TBQPH) molecule was synthesized by a simple Schiff base reaction, which contains six carbonyl groups and six imine groups. The reaction mechanism of TBQPH was systematically analyzed by the various *ex-situ* characterization techniques and density functional theory (DFT) calculation, unveiling the reaction sequence of C=O bonds and C=N bonds in companion with the combination/release of hydrogen ions during charging/discharging. As a result, the TBQPH electrode exhibits a specific capacity of 455.8 mAh g^{-1} at 0.3 A g^{-1} (energy efficiency up to 88.5% based on the theoretical capacity of 515 mAh g^{-1}) and ultra-long cycle stability (capacity retention of 78% after 10,000 cycles at 10 A g^{-1}). Finally, the sources for the excellent electrochemical performances of the TBQPH electrodes were detailedly analyzed.

2. Results and discussion

The synthetic route of TBQPH is presented in Fig. 1a, which employs a dehydration condensation reaction of ketones and amines [23]. The detailed synthesis processes are described in the Supporting Information. In brief, a mixture of hexaketocyclohexane octahydrate (HKH) and 2,3-diaminonaphthalene-1,4–dione (DND) (1:3, mol%) in methanol/acetic acid (1:1, v%) solution was stirred at 65 °C for 12h. Then, the mixture was filtered and washed with acetone, ethanol, and water to obtain a dark yellow product. The product is insoluble in solvents such as ethanol, H_2O, DMSO, dichloromethane (CH_2Cl_2), chloroform ($CHCl_3$), tetrahydrofuran (THF), and acetone. The structural component of TBQPH was confirmed by ^1H NMR (Fig. S1, Supporting Information), ^{13}C NMR (Fig. S2), Fourier transform infrared (FT-IR) spectroscopy, X-ray photoelectron spectroscopy (XPS), Raman spectrum, and thermal gravimetric analysis (TGA).

In FT-IR spectrum(Figs. 1b and S3a), Two strong vibration peaks appear at 1695 cm^{-1} and 1586 cm^{-1}, which corresponds to the C=O and C=N groups of TBQPH, respectively [40]. The carbonyl groups (1640 cm^{-1}) of DND shifted to a higher wavenumber (1695 cm^{-1}) after the condensation reaction due to the diminution of the electron-withdrawing effect of -NH_2. The carbonyl peak of HKH disappeared after the reaction. Moreover, no stretching vibration peak and in-plane bending vibration peak of N-H bonds are observed, which indirectly indicates the formation of the C=N bond. In addition, XPS was used to detect the chemical states of C, N, and O elements in the TBQPH. The full survey XPS spectrum in Fig. S4 indicates that there are three distinct peaks near 282, 397, and 529 eV, corresponding to C 1s, N 1s, and O 1s, respectively. The high-resolution C 1s XPS spectra (Fig. 1c) were further analyzed by the peak fitting calculation, and the four peaks at approximately 284.6, 285.7, 286.0, and 287.4 eV could be ascribed to C–C, C–N, C=N, and C=O bonds, respectively. The high-resolution N 1s peak at 399.4 eV is divided into two peaks, which are attributed to the bonds of C=N (399.2 eV) and C-N (399.6 eV), respectively [41]. For the high-resolution O 1s XPS spectrum, the peak at 531.4 eV can be assigned to the C=O bond [42]. These results further illustrate the formation of C=N bonds. Besides, the Raman spectrum (Fig. S5) also confirmed that a distinct peak of the C=O bond was observed at 1683 cm^{-1}. The crystal structure of TBQPH was clarified by X-ray diffraction (XRD) as shown in Fig. S6. In addition to a few obvious weak peaks, two sharp peaks can be observed at 5.9° and 27.7°. The peak at 27.7° may be due to the π-π stacking structure between molecular layers, which corresponds to a layer distance of 3.2 Å The XRD results reveal that the TBQPH exhibits a clear stacking arrangement of crystals. TGA (Fig. S7) shows that the TBQPH possesses high thermal stability under argon atmosphere.

The scanning electron microscope (SEM) was carried out to characterize the micromorphology of the pristine TBQPH sample

(Fig. 1d). TBQPH is composed of irregular nanorods with a diameter of about 150 nm, which is conducive to large-area contact with conductive additives and full infiltration with electrolytes. The hydrophilicity of the electrode sheet was explored through the contact angle test (Fig. S8). Two included angles less than 86° are formed between the electrode sheet and the aqueous solution, indicating that the TBQPH electrode has a good solvent affinity. Transmission electron microscopy (TEM) and energy dispersive spectroscopy (EDS) element mapping of the pristine sample (Fig. 1e) reveals that the elements C, N, and O are evenly distributed on the TBQPH. DFT calculation was performed to investigate the energy levels and energy gap (ΔE_{gap}) of TBQPH under simulated vacuum conditions (Fig. 1f). The calculation results show that the highest occupied molecular orbital (HOMO) and the lowest unoccupied molecular orbital (LUMO) energy levels of TBQPH are −7.13 and −3.49 eV, respectively. Therefore, the corresponding ΔE_{gap} is 3.64 eV The lower HOMO/LUMO energy levels and narrow bandgap provide a good foundation for the inherent electronic conductivity of TBQPH, which is beneficial to improving the electrochemical performances of TBQPH as the electrode [43,44].

To examine the electrochemical performances of TBQPH, the cathodes based on TBQPH were prepared by mixed with conductive additive (Ketjen black) and the binder (PTFE). The electrochemical performances of TBQPH are evaluated by cyclic voltammetry (CV) and galvanostatic charge-discharge (GCD). As shown in Fig. S9, CV curves of TBQPH electrode at the first three cycles were investigated at a scan rate of 0.2 mV s^{-1} in the voltage range of 0.2–1.7 V. The CV curves of TBQPH display six reduction peaks, implying that the TBQPH electrode integrated by carbonyl and amine groups may adopt a multi-step reaction mechanism. The initial discharged capacity of the TBQPH electrode can reach 455.8 mAh g^{-1} at 0.3 A g^{-1} (Fig. 2a), which is the highest level as we know in the aqueous ZOBs (Table S1)[30,34,35,37,45–47]. Furthermore, multiple discharged/charged platforms are also observed on the GCD curves, which is consistent with the above CV curves.

To further realize the storage mechanism of TBQPH electrodes, *ex-situ* FT-IR, XPS, XRD, SEM, and NMR characterizations were carried out during charging/discharging. Firstly, the *ex-situ* FT-IR spectra (Fig. 2b) of TBQPH electrodes at different marked points were detected. The peaks at 1688 cm^{-1} and 1579 cm^{-1} disappear and appear regularly at cycling, demonstrating that the C=O bond and C=N bond are the active centers of electrochemical reactions. During the discharging process, the peak of the C=O disappeared earlier than that of the C=N, indicating that the C=O was the preferential reduced. Meanwhile, the peak of the C=N appeared earlier than the peak of the C=O during the charging process, indicating that the C=N is the preferential oxidized. More importantly, a large broad peak appears at 3300 cm^{-1} after discharging to 0.2 V, which is attributed to the formation of the -OH bond. This result indicates that the C=O bonds of TBQPH are combined with H^+ during the discharge process. *Ex-situ* XPS (Fig. 2c) was performed to further investigate the variations in the chemical bond of TBQPH electrodes during charging/discharging. Here, the XPS spectra of the TBQPH powder (Fig. 1c) are taken as the XPS spectra of the TBQPH electrode in the initial state. The C 1s XPS spectrum of the TBQPH electrode after being discharged to 0.2 V show that the intensities of the C=N bands at 286.0 eV and the C=O bands at 287.4 eV decreased significantly, while the intensities of the C-N at 285.9 eV and the C-O bands at 286.5 eV increased, indicating that the C=N bonds and C=O bonds were transformed to the C-N bonds and C-O bonds, respectively. When charging to 1.7 V, the peak of the C-O band disappears, while the peak of the C=O band reappears at 287.6 eV. In addition, The C=N peak in the N 1s XPS spectra also disappears and appears during discharging/charging, accompanied by the appearance/disappearance of the N-H peak as well as the increase/decrease of the C-N peak. Similarly, the O 1s XPS spectrum of the TBQPH is divided into two peaks after being discharged to 0.2 V, which are assigned to the C-O bond (531.3 eV) and the O-H bond (532.0 eV), indicating the formation of the C-O bond and the O-H bond. In the charging state, the peaks of the C-O bond and O-H bond disappeared and the peak of the C=O bond reappears, indicating the reversible transformation from the C-O bond to carbonyl groups (C=O). The *ex-situ* XPS spectra further show that both C=O bonds and C=N bonds can be utilized as reversible redox sites.

In addition, the *ex-situ* XRD pattern of the TBQPH electrode (Fig. S10) shows that the peak of 5.9° shifts to 5.4° when discharged to 0.2 V, which may be attributed to that the combination of the TBQPH and H^+ enlarges the distance between molecules. The peak at 27.7° was shifted to 27°, indicating that the interlayer spacing between molecules was slightly enlarged. The peaks returned to the pristine state after being charged to 1.7 V, demonstrating the good reversibility of TBQPH during the charging/discharging. Besides, a strong peak was detected at about 10° during discharging, which may be attributed to the formation of $Zn_4SO_4(OH)_6{\bullet}xH_2O$ crystals [35]. Furthermore, the *ex-situ* SEM was employed to survey the morphological changes on the surface of the TBQPH electrode (Fig. S11). The pristine electrode showed a flat surface. After discharge to 0.2 V, a large amount of lamellar-like structures appeared on the surface of the TBQPH electrode, which may be the $Zn_4SO_4(OH)_6{\bullet}xH_2O$ crystals. During the discharge process, the redox groups of TBQPH combine with the H^+ generated by the decomposition of water to complete the charge transfer. At the same time, the decomposition of water will also produce a large amount of OH^-. These OH^- will combine with $ZnSO_4$ to form water-insoluble $Zn_4SO_4(OH)_6{\bullet}xH_2O$ and deposit on the surface of the TBQPH electrode to form lamellar crystals. Besides, the zinc anode loses electrons and transforms into zinc ions to achieve the purpose of balancing the charge. After the charging process, the surface of the TBQPH electrode returned to a flat state. The disappearance of the peak at 10° at charging state is due to the combination of OH^- in the crystal and H^+ released from the TBQPH electrode, resulting in soluble zinc sulfate and H_2O. To further verify that hydrogen ions participate in the electrochemical reaction, the discharged TBQPH electrode was characterized by using liquid ^1H NMR (Fig. S12). The TBQPH electrode discharged to 0.2 V was taken out, and the electrode piece was dissolved in mild DMSO–d_6 by ultrasonic treatment. Compared with the ^1H NMR spectrum of TBQPH powder, the spectrum of discharged TBQPH electrode obviously has two extra peaks, which may be the peaks of -OH and –NH, respectively. The discharged TBQPH electrode still has poor solubility in DMSO–d_6, so the intensity of the peaks is not strong. But it is enough to illustrate the formation of -OH and -NH bonds. The liquid ^1H NMR spectrum provides direct evidence for hydrogen ion insertion/extraction. Various *ex-situ* results show that C=O bonds and C=N bonds are acted as electrochemical active centers to reversibly react with H^+ accompanied by the formation/decomposition of $Zn_4SO_4(OH)_6{\bullet}xH_2O$ on the surface of the TBQPH electrode.

To further investigate the discharged mechanism of the TBQPH electrode, DFT calculations were performed to investigate the structural evolution of a TBQPH molecule during the reaction with H^+ [35,48]. First, the electrochemically active sites of TBQPH were speculated by molecular electrostatic potential (MESP). As shown in Fig. 2d, the positive MESP values appear on the surfaces of C and H, which indicates that they are electrophilic centers and are more inclined to react with nucleophiles. The negative MESP values only appeared in the vicinity of O and N, indicating that they have strong electronegativity and more inclined to react with electrophiles. Generally, the regions with negative MESP values are more attractive to cations [41,46]. Therefore, carbonyl groups and pyrazines with higher negative MESP values are considered to be

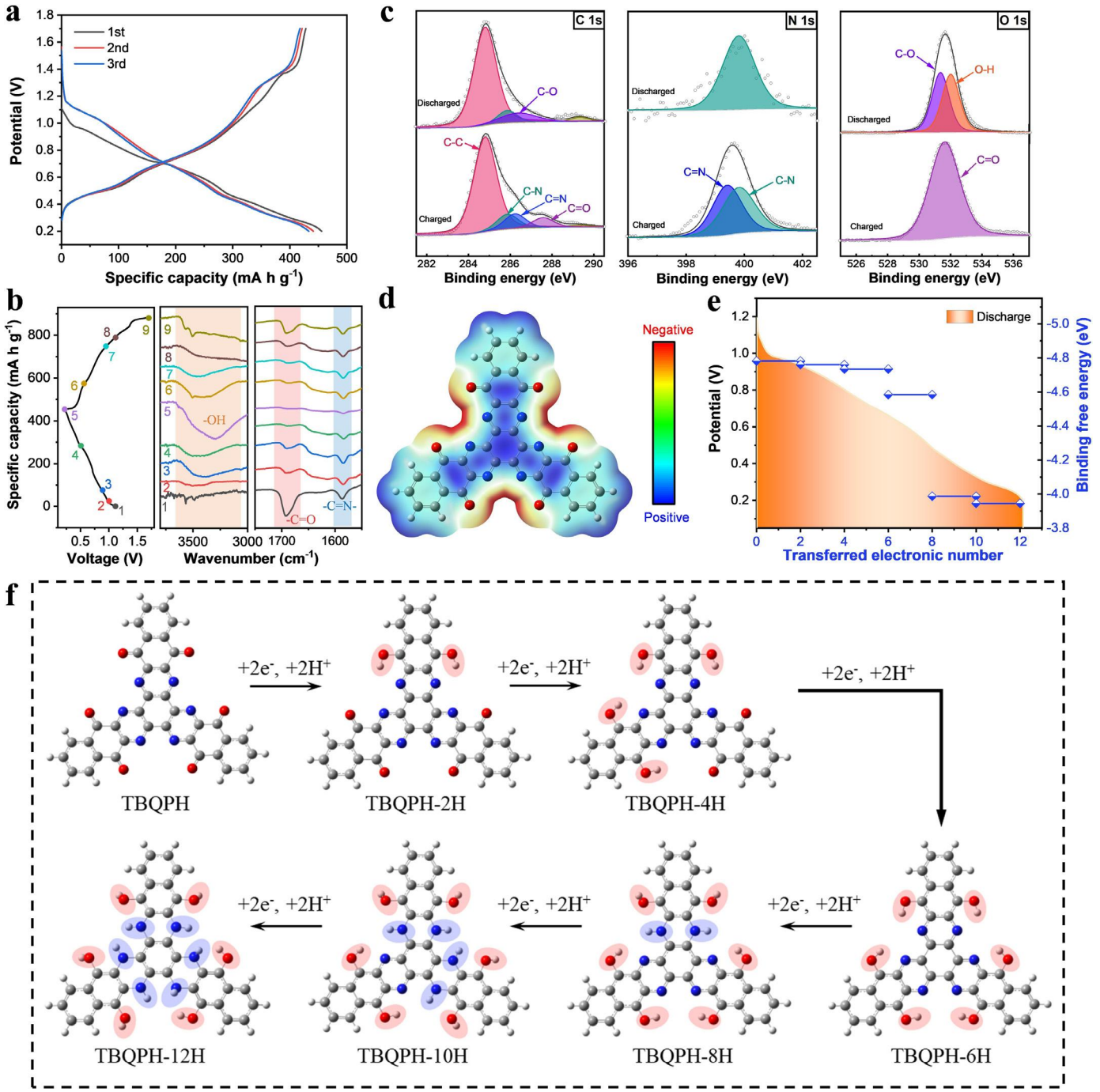

Fig. 2. (a) The GCD profile at 0.3 A g^{-1}. (b) The GCD curves of the first cycle at 300 mAh g^{-1} and *ex-situ* FT-IR spectra of TBQPH electrode at different marked points. (c) *Ex-situ* XPS spectra of C 1 s, N 1 s, and O 1 s at the 1st discharged and charged. (d) MESP distribution of TBQPH molecule. (e) The redox potential (orange) and calculated binding free energies (blue) of TBQPH electrode. (f) The proposed 12-electron storage mechanism and optimized structures of TBQPH electrodes by DFT calculation (For interpretation of the references to color in this figure legend, the reader is referred to the web version of this article.).

redox centers that bind to H^+ in the discharge process. This result is consistent with the conclusions of *ex-situ* FT-IR and *ex-situ* XPS. Furthermore, the protonation path of TBQPH during discharging is calculated according to the minimum energy principle. The protonation processes of TBQPH are assumed to be six steps, each of which combines two electrons and two H^+. The optimal structures and Gibbs free energies of the protonated TBQPH molecules in each step are shown in Fig. 2f and Fig. S13, respectively. According to the results of *ex-situ* FT-IR, the carbonyl group reacts preferentially with H^+ because the reactivity of the C=O bond is higher than that of the C=N bond. Therefore, hydrogen ions mainly react with three pairs of carbonyl groups in the first three steps and bond with pyrazines in the last three steps. The initial TBQPH molecule produced a TBQPH-12H molecule combining 12 electrons and 12 hydrogen ions after the six-step reaction. The binding free energies of TBQPHs were calculated through the Gibbs free energies of structural optimization to study the relationship with the oxidation–reduction potential (Fig. 2e). As the binding number of the TBQPH with hydrogen ions increases, the binding free energy gradually decreases. This trend is basically the same as the discharge potential. The above result also further proves that the hypothesized protonation process is the most likely reaction route.

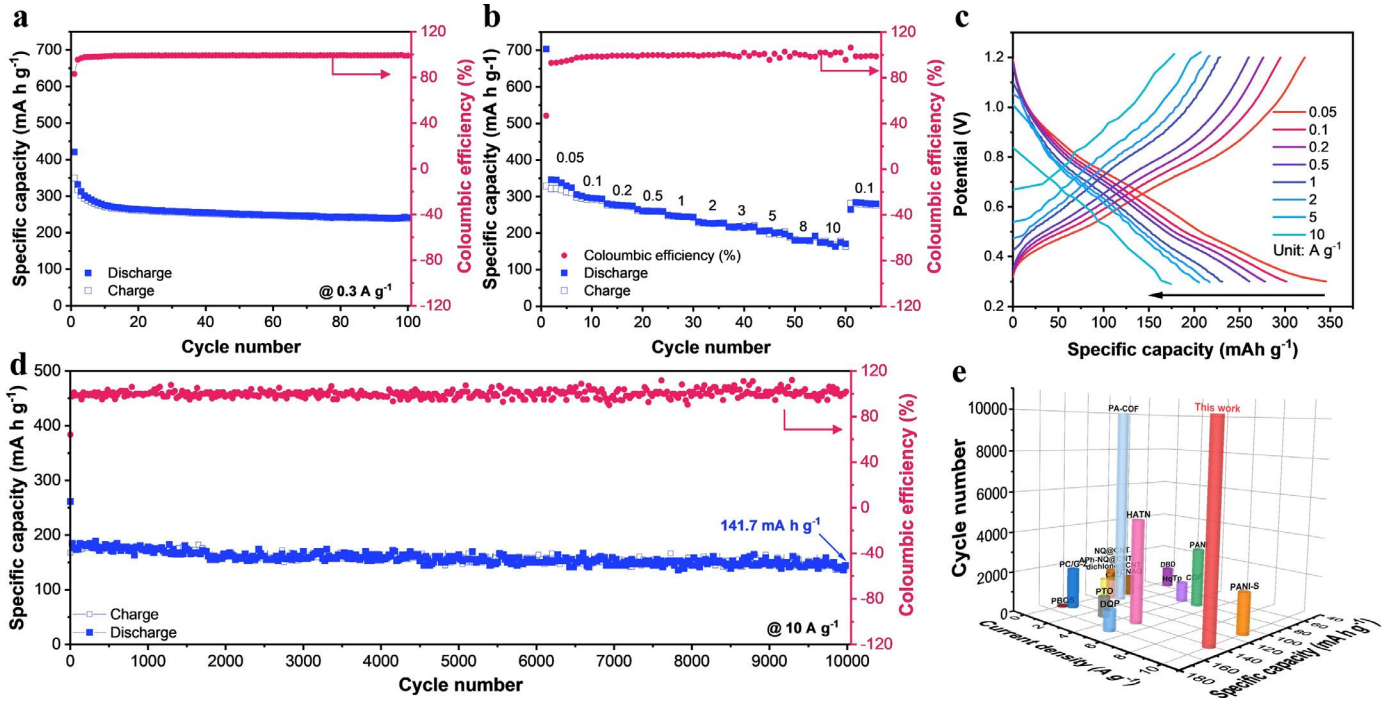

Fig. 3. (a) Cycle performance of TBQPH electrode at 0.3 A g^{-1}. (b) Rate capability of TBQPH electrode. (c) The GCD profile of TBQPH electrodes at various current rates. (d) Long-term cycle performances at 10 A g^{-1}. (e) Long cycling performance comparison of TBQPH versus previously reported ZOBs.

In addition, when pyrazines are combined with hydrogen ions, the structure of TBQPH generates a slight twist of approximately 12° (Fig. S14). The change from the double bonds of the N atoms to the single bonds is the main reason for the transformation from the plane to the triangular pyramid configuration. Compared with the original TBQPH, the twisted TBQPH-12H molecules are loosely stacked, which may be the root reason for the increase of interlayer spacing in the discharged state.

The cycling performances and rate capability of the TBQPH electrodes in a voltage range of 0.2 - 1.7 V were also studied. Under a current density of 0.3 A g^{-1}, the specific capacity decays slowly and continuously from 455 to 300 mAh g^{-1} within 100 cycles (Fig. S15). The rate capability of TBQPH electrodes is shown in Fig. S16. TBQPH delivers capacities of 455, 360, 328, 297, 281, 266, 247, 225, and 193 mAh g^{-1} under increased current rates of 0.05, 0.1, 0.2, 0.5, 1, 2, 3, 5, and 8 A g^{-1}, respectively. Moreover, even at a current density of 10 A g^{-1}, TBQPH electrodes still display a high capacity of about 177 mAh g^{-1}, which is about 49% of that at 0.1 A g^{-1}. The rate capability exceeds most of the previously reported cathode materials in ZOBs (Fig. S17). The above cycling performance and rate performance both show a slight capacity decay. To find out the cause of performance instability, we conducted solubility tests of the electrode sheet. First, the initial electrode sheet was soaked in a 2 M $ZnSO_4$ electrolyte for 15 days (Fig. S18a). There is no obvious color change in the solution, indicating that the TBQPH electrode is insoluble in the electrolyte in the charged state. Subsequently, we disassembled the button battery discharged to 0.2 V, and there was no phenomenon of electrode dissolution (Fig. S18b). Therefore, the capacity decay is not caused by the dissolution of the electrode. According to previous reports[49–51], the original stable structure of the carbonyl-containing organic material may become relatively unstable during the over-discharge/charge processes. The decay of TBQPH electrode cycle performance may be due to excessive charge/discharge, which reduces the reversibility of active groups.

In order to obtain better stability, the voltage range was adjusted from 0.2 - 1.7 V to 0.3 - 1.2 V (**Fig. 3**). As a result, the capacity remains almost constant after 30 cycles at 0.3 A g^{-1} (Fig. 3a). Rate performance of TBQPH in the voltage range of 0.3 - 1.2 V was also measured (Fig. 3b and c). The discharge capacities of TBQPH electrodes at current densities of 0.05, 0.1, 0.2, 0.5, 1, 2, 3, 5, and 8 A g^{-1} are 346, 305, 277, 260, 245, 226, 218, 201, and 180 mAh g^{-1}, respectively. It is worth mentioning that the capacity difference before and after the adjustment is only about 7 mAh g^{-1} under a current rate of 10 A g^{-1}. To verify the stability of TBQ electrodes, the long-term cycling performances were further evaluated at 5 A g^{-1} and 10 A g^{-1}. At 5 A g^{-1}, a high reversible capacity of 152.8 mAh g^{-1} is obtained after 10,000 cycles, and the coulombic efficiency remains nearly 100% (Fig. S19). More importantly, the TBQPH electrode maintains a high reversible capacity of 141.7 mAh g^{-1} after 10,000 cycles at 10 A g^{-1} (Fig. 3d), and the average capacity decay rate is only 0.0022% per cycle. This excellent cycling stability exceeds most of the previously reported organic cathode materials in Zn-organic batteries (Fig. 3e).

To analyze the kinetics of the TBQPH electrode, the CV curves at different scan rates were measured from 0.1 to 1.0 mV s^{-1}. As shown in **Fig. 4a**, with the acceleration of scanning rate, the three pairs of redox peaks of the CV curves become more and more distinct. Meanwhile, with the increase of scan rates, the oxidation peaks shift to high voltages, while the reduction peaks shift to low voltages. The capacitive contribution of TBQPH electrodes was qualitatively analyzed, according to the Eq. (1) [52–54]:

$$i = av^b \quad (1)$$

where i is the peak current, v is the scan rate. The b value can be calculated by plotting the logarithmic relationship of i and v. Generally, when the b value is close to 0.5, the electrochemical reaction is the diffusion-controlled Faraday process. On the contrary, when the b value is close to 1, the charge storage process is capacitive. All the b values of the anodic and cathodic peaks are both close to 1 (Fig. 4b), indicating that the electrochemical reaction of the TBQPH electrode is dominated by the capacitive process and

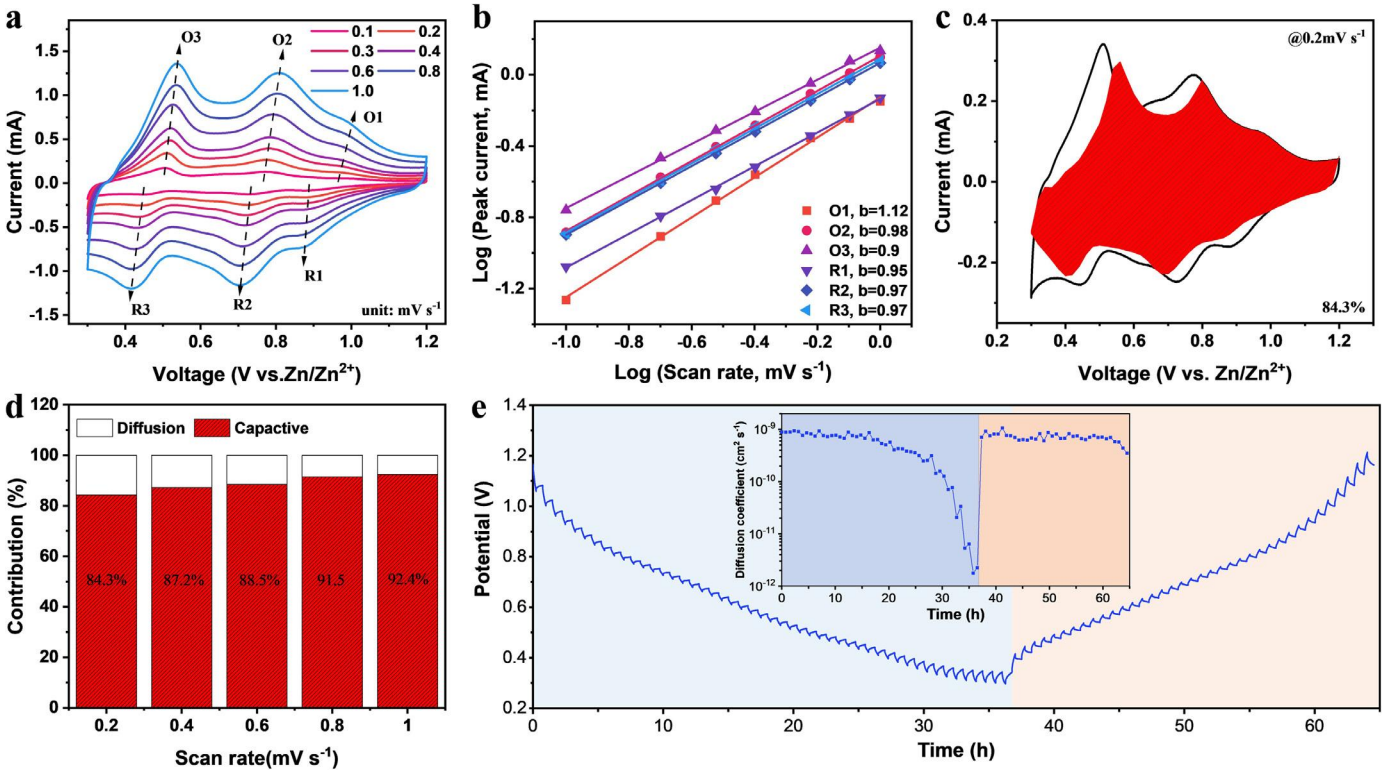

Fig. 4. Kinetic analyses of TBQPH electrodes. (a) CV curves of TBQPH at various scan rates. (b) Linear fitting plots of log(i) and log(v) at cathodic and anodic peaks (i: peak current, v: scan rate). (c) Capacitive contribution at a scan rate of 0.2 mV s^{-1}. (d) Capacitive-controlled and diffusion-limited capacity contribution at different scan rates. (e) GITT curves of TBQPH electrodes at a repeating constant current pulse of 30 mA g^{-1} (inset shows the calculated H^+ diffusion coefficients) (For interpretation of the references to color in this figure, the reader is referred to the web version of this article.).

possesses fast kinetics. The capacitive charge contribution can be distinguished according to the following Eq. (2):[52–54]

$$i = k_1 v + k_2 v^{1/2} \quad (2)$$

The current response i is proportional to v and $v^{1/2}$, which can be considered as a collection of diffusion-controlled and capacitive processes, respectively. Thought calculating k_1 and k_2 at fixed potentials, the capacity contributions of two processes can be quantified. The response curve of the capacitive contribution (red shadow area) and the total current are shown in Fig. 4c. The capacitive contribution rate of the TBQPH electrode reached 84.3% at a scan rate of 0.2 mV s^{-1}. As the scan rate increases, the rate of the capacitive control process gradually increases (Fig. 4d). At a scan rate of 1 mV s^{-1}, the capacitive contribution proportion reaches the highest value of 92.4%. The small size and irregular rod morphology of TBQPH material may play a vital role in the highly capacitive contribution [55–57]. A higher proportion of capacitive contribution is beneficial to the excellent kinetics exhibited during charge and discharge cycles.

To further reveal the diffusion kinetics of hydrogen ions, the ion diffusion coefficients are calculated by the galvanostatic intermittent titration technique (GITT). In the initial stage of discharge, the diffusion coefficient of hydrogen ions basically maintained at about 8×10^{-10} cm^2 s^{-1} (Fig. 4e). At the end of the discharge, the diffusion coefficient quickly drops to 1.7×10^{-12} cm^2 s^{-1}. Similarly, the same tendency also appeared during charging. The stable ion diffusion coefficient may be one of the reasons for the excellent rate performance.

The resistance characteristics of the TBQPH electrode during long cycles were also investigated by electrochemical impedance spectroscopy (EIS). **Fig. 5a** shows the EIS data of TBQPH electrode at 1 A g^{-1}after different cycles. The battery based on the TBQPH cathode and Zn anode has a large initial impedance. In the first 10 cycles, the charge-transfer resistance (R_{ct}) of the TBQPH electrode gradually decreased, indicating that the ion diffusion channel was greatly improved with the activation of the first few cycles [58,59]. From the 10th to 1000th circles, the R_{ct} basically maintains a lower level, which may be an important factor for obtaining excellent long-term cycling stability [60]. To analyze the self-discharge behavior, the TBQPH electrode was charged to 1.2 V with a current density of 0.1 A g^{-1} and stood for 24 h (Fig. 5b). After that, a discharge capacity of 258.1 mAh g^{-1} is still obtained, which is basically the same as the charge capacity, indicating that the self-discharge behavior can be ignored. The excellent self-discharge behavior is due to the stability of the TBQPH electrode in the charged state, so it will not be decomposed by the influence of water and air in the battery [41]. Based on the above results, it is confirmed that the excellent electrochemical performances of the TBQPH electrode are attributed to the high proportion of capacitance effect, high ion diffusion coefficient, and low charge transfer resistance.

3. Conclusion

In summary, we designed a high-capacity organic molecule namely TBQPH with dual redox sites of carbonyl as well as pyrazine and applied it as a cathode material for aqueous ZOBs. A high capacity of 455.8 mAh g^{-1} was delivered by the TBQPH electrode under a current density of 0.3 A g^{-1}. Various *ex-situ* characterization and DFT calculation results indicate that the TBQPH electrode is combined with H^+ during charge storage. Also, it has been demonstrated that both the C=O bond and the C=N bond are the redox centers of electrochemical reactions. The carbonyl group activity is higher than that of pyrazine during discharge. At a current density of 10 A g^{-1}, the TBQPH electrode still exhibits a capacity of 141.7 mAh g^{-1} after 10,000 cycles with an average capacity decay rate of only 0.0022% per cycle. These excellent electrochemical

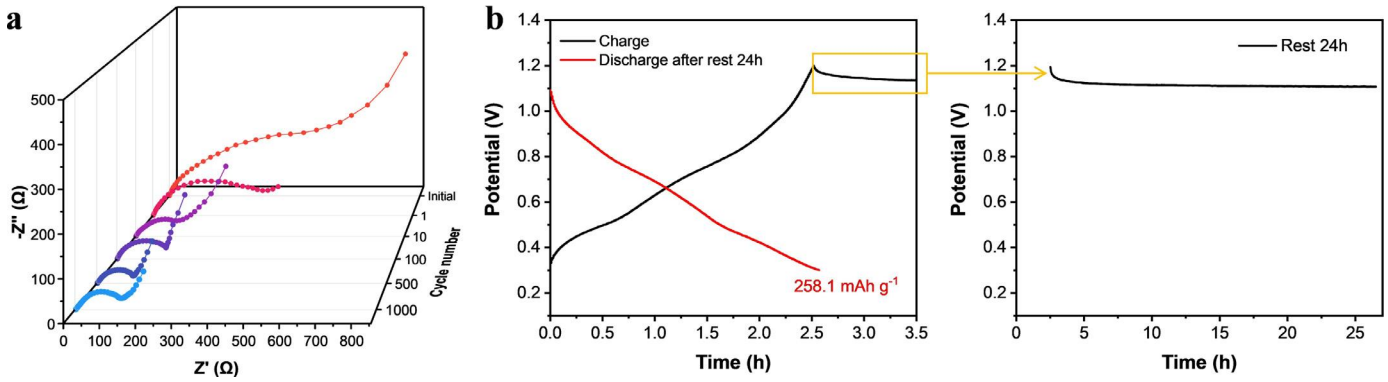

Fig. 5. (a) Nyquist plots of TBQPH electrodes measured at different cycles at 1 A g^{-1}. (b) Self-discharge behaviors under 100 mA g^{-1}. When charged to 1.2 V and then discharged to 0.3 V after 24 h rest.

performances are attributed to the faster ion transport kinetics and lower charge transfer resistance of the TBQPH electrode. This work provides effective guidance for the research of organic electrode materials with multiple redox sites and long cycle life in the next generation of zinc-ion batteries.

Declaration of Competing Interest

The authors declare no conflict of interest

Acknowledgments

Y. An and Y. Liu contributed equally to this work. This work was supported by the National Key Research and Development Program of China (2017YFE0127600), National Natural Science Foundation of China (51521001, 51972259, and 51602239), Foshan Xianhu Laboratory of the Advanced Energy Science and Technology Guangdong Laboratory (XHT2020-003), Programme of Introducing Talents of Discipline to Universities (B17034), the Natural Science Foundation of Hubei Province (2019CFA001).

Supplementary materials

Supplementary material associated with this article can be found, in the online version, at doi:10.1016/j.electacta.2021.139620.

References

[1] D. Larcher, J.M. Tarascon, Towards greener and more sustainable batteries for electrical energy storage, Nat. Chem. 7 (1) (2015) 19–29, doi:10.1038/nchem.2085.
[2] Y. Yusran, Q. Fang, V. Valtchev, Electroactive covalent organic frameworks: design, synthesis, and applications, Adv. Mater. 32 (44) (2020) 2002038, doi:10.1002/adma.202002038.
[3] M. Chen, Q. Liu, Z. Hu, Y. Zhang, G. Xing, Y. Tang, S.L. Chou, Designing advanced vanadium-based materials to achieve electrochemically active multi-electron reactions in sodium/potassium-ion batteries, Adv. Energy Mater. 10 (42) (2020) 2002244, doi:10.1002/aenm.202002244.
[4] J. Yang, P. Xiong, Y. Shi, P. Sun, Z. Wang, Z. Chen, Y. Xu, Rational molecular design of benzoquinone-derived cathode materials for high-performance lithium-ion batteries, Adv. Funct. Mater. 30 (15) (2020) 1909597, doi:10.1002/adfm.201909597.
[5] B. Yong, D. Ma, Y. Wang, H. Mi, C. He, P. Zhang, Understanding the design principles of advanced aqueous zinc-ion battery cathodes: from transport kinetics to structural engineering, and future perspectives, Adv. Energy Mater. 10 (45) (2020) 2002354, doi:10.1002/aenm.202002354.
[6] S. Tan, F. Xiong, J. Wang, Q. An, L. Mai, Crystal regulation towards rechargeable magnesium battery cathode materials, Mater. Horiz. 7 (8) (2020) 1971–1995, doi:10.1039/d0mh00315h.
[7] F. Xiong, S. Tan, X. Yao, Q. An, L. Mai, Crystal defect modulation in cathode materials for non-lithium ion batteries: progress and challenges, Mater. Today 45 (2021) 169–190, doi:10.1016/j.mattod.2020.12.002.
[8] F. Wang, O. Borodin, T. Gao, X.L. Fan, W. Sun, F.D. Han, A. Faraone, J.A. Dura, K. Xu, C.S. Wang, Highly reversible zinc metal anode for aqueous batteries, Nat. Mater. 17 (6) (2018) 543–549, doi:10.1038/s41563-018-0063-z.
[9] M. Huang, X. Wang, J. Meng, X. Liu, X. Yao, Z. Liu, L. Mai, Ultra-fast and high-stable near-pseudocapacitance intercalation cathode for aqueous potassium-ion storage, Nano Energy 77 (2020) 105069, doi:10.1016/j.nanoen.2020.105069.
[10] J.H. Jo, Y. Aniskevich, J. Kim, J.U. Choi, H.J. Kim, Y.H. Jung, D. Ahn, T.Y. Jeon, K.S. Lee, S.H. Song, H. Kim, G. Ragoisha, A. Mazanik, E. Streltsov, S.T. Myung, New insight on open-structured sodium vanadium oxide as high-capacity and long life cathode for Zn-Ion storage: structure, electrochemistry, and first-principles calculation, Adv. Energy Mater. 10 (40) (2020) 2001595, doi:10.1002/aenm.202001595.
[11] W. Yang, X. Du, J. Zhao, Z. Chen, J. Li, J. Xie, Y. Zhang, Z. Cui, Q. Kong, Z. Zhao, C. Wang, Q. Zhang, G. Cui, Hydrated eutectic electrolytes with ligand-oriented solvation shells for long-cycling zinc-organic batteries, Joule 4 (7) (2020) 1557–1574, doi:10.1016/j.joule.2020.05.018.
[12] L. Zhang, L. Chen, X. Zhou, Z. Liu, Towards high-voltage aqueous metal-ion batteries beyond 1.5 V: the zinc/zinc hexacyanoferrate system, Adv. Energy Mater. 5 (2) (2015) 1400930, doi:10.1002/aenm.201400930.
[13] Q. Yang, F. Mo, Z. Liu, L. Ma, X. Li, D. Fang, S. Chen, S. Zhang, C. Zhi, Activating C-coordinated iron of iron hexacyanoferrate for Zn hybrid-ion batteries with 10 000 cycle lifespan and superior rate capability, Adv. Mater. 31 (32) (2019) 1901521, doi:10.1002/adma.201901521.
[14] D. Kundu, B.D. Adams, V. Duffort, S.H. Vajargah, L.F. Nazar, A high-capacity and long-life aqueous rechargeable zinc battery using a metal oxide intercalation cathode, Nat. Energy 1 (2016) 16119, doi:10.1038/Nenergy.2016.119.
[15] P. He, M. Yan, G. Zhang, R. Sun, L. Chen, Q. An, L. Mai, Layered VS_2 nanosheet-based aqueous Zn ion battery cathode, Adv. Energy Mater. 7 (11) (2017) 1601920, doi:10.1002/aenm.201601920.
[16] N. Zhang, F. Cheng, J. Liu, L. Wang, X. Long, X. Liu, F. Li, J. Chen, Rechargeable aqueous zinc-manganese dioxide batteries with high energy and power densities, Nat. Commun. 8 (1) (2017) 405, doi:10.1038/s41467-017-00467-x.
[17] J. Huang, Z. Wang, M. Hou, X. Dong, Y. Liu, Y. Wang, Y. Xia, Polyaniline-intercalated manganese dioxide nanolayers as a high-performance cathode material for an aqueous zinc-ion battery, Nat. Commun. 9 (1) (2018) 2906, doi:10.1038/s41467-018-04949-4.
[18] J. Huang, Z. Guo, Y. Ma, D. Bin, Y. Wang, Y. Xia, Recent progress of rechargeable batteries using mild aqueous electrolytes, Small Methods 3 (1) (2019) 1800272, doi:10.1002/smtd.201800272.
[19] X. Jia, C. Liu, Z. Neale, J. Yang, G. Cao, Active materials for aqueous zinc ion batteries: synthesis, crystal structure, morphology, and electrochemistry, Chem. Rev. 120 (15) (2020) 7795–7866, doi:10.1021/acs.chemrev.9b00628.
[20] J. Wang, A.E. Lakraychi, X. Liu, L. Sieuw, C. Morari, P. Poizot, A. Vlad, Conjugated sulfonamides as a class of organic lithium-ion positive electrodes, Nat. Mater. 20 (5) (2020) 665–673, doi:10.1038/s41563-020-00869-1.
[21] M.R. Tuttle, S.T. Davis, S. Zhang, Synergistic effect of hydrogen bonding and π–π stacking enables long cycle life in organic electrode materials, ACS Energy Lett. 6 (2) (2021) 643–649, doi:10.1021/acsenergylett.0c02604.
[22] Y. Ding, X. Guo, Y. Qian, L. Zhang, L. Xue, J.B. Goodenough, G. Yu, A liquid-metal-enabled versatile organic alkali-ion battery, Adv. Mater. 31 (11) (2019) 1806956, doi:10.1002/adma.201806956.
[23] C. Peng, G.H. Ning, J. Su, G. Zhong, W. Tang, B. Tian, C. Su, D. Yu, L. Zu, J. Yang, M.F. Ng, Y.S. Hu, Y. Yang, M. Armand, K.P. Loh, Reversible multi-electron redox chemistry of π-conjugated N-containing heteroaromatic molecule-based organic cathodes, Nat. Energy 2 (7) (2017) 17074, doi:10.1038/nenergy.2017.74.
[24] A. Jouhara, N. Dupre, A.C. Gaillot, D. Guyomard, F. Dolhem, P. Poizot, Raising the redox potential in carboxyphenolate-based positive organic materials via cation substitution, Nat. Commun. 9 (1) (2018) 4401, doi:10.1038/s41467-018-06708-x.
[25] T. Sun, J. Xie, W. Guo, D.S. Li, Q. Zhang, Covalent-organic frameworks: advanced organic electrode materials for rechargeable batteries, Adv. Energy Mater. 10 (19) (2020), doi:10.1002/aenm.201904199.
[26] P. Poizot, J. Gaubicher, S. Renault, L. Dubois, Y. Liang, Y. Yao, Opportunities and challenges for organic electrodes in electrochemical energy storage, Chem. Rev. 120 (14) (2020) 6490–6557, doi:10.1021/acs.chemrev.9b00482.
[27] Q. Yu, Z. Xue, M. Li, P. Qiu, C. Li, S. Wang, J. Yu, H. Nara, J. Na, Y. Yamauchi, Elec-

trochemical activity of nitrogen-containing groups in organic electrode materials and related improvement strategies, Adv. Energy Mater. 11 (7) (2021) 2002523, doi:10.1002/aenm.202002523.
[28] K. Qin, J. Huang, K. Holguin, C. Luo, Recent advances in developing organic electrode materials for multivalent rechargeable batteries, Energy Environ. Sci. 13 (11) (2020) 3950–3992, doi:10.1039/d0ee02111c.
[29] J. Xie, Q. Zhang, Recent progress in multivalent metal (Mg, Zn, Ca, and Al) and metal-ion rechargeable batteries with organic materials as promising electrodes, Small 15 (15) (2019) e1805061, doi:10.1002/smll.201805061.
[30] Z. Guo, Y. Ma, X. Dong, J. Huang, Y. Wang, Y. Xia, An environmentally friendly and flexible aqueous zinc battery using an organic cathode, Angew. Chem. Int. Ed. 57 (36) (2018) 11737–11741, doi:10.1002/anie.201807121.
[31] Q. Zhao, W. Huang, Z. Luo, L. Liu, Y. Lu, Y. Li, L. Li, J. Hu, H. Ma, J. Chen, High-capacity aqueous zinc batteries using sustainable quinone electrodes, Sci. Adv. 4 (3) (2018) eaao1761, doi:10.1126/sciadv.aao1761.
[32] T. Sun, Z.J. Li, Y.F. Zhi, Y.J. Huang, H.J. Fan, Q. Zhang, Poly(2,5-Dihydroxy-1,4-Benzoquinonyl Sulfide) as an efficient cathode for high-performance aqueous zinc–organic batteries, Adv. Funct. Mater. 31 (16) (2021) 2010049, doi:10.1002/adfm.202010049.
[33] J. Xie, F. Yu, J. Zhao, W. Guo, H.L. Zhang, G. Cui, Q. Zhang, An irreversible electrolyte anion-doping strategy toward a superior aqueous Zn-organic battery, Energy Storage Mater. 33 (2020) 283–289, doi:10.1016/j.ensm.2020.08.027.
[34] Y. Wang, C. Wang, Z. Ni, Y. Gu, B. Wang, Z. Guo, Z. Wang, D. Bin, J. Ma, Y. Wang, Binding zinc ions by carboxyl groups from adjacent molecules toward long-life aqueous zinc-organic batteries, Adv. Mater. 32 (16) (2020) 2000338, doi:10.1002/adma.202000338.
[35] Z. Tie, L. Liu, S. Deng, D. Zhao, Z. Niu, Proton insertion chemistry of a zinc-organic battery, Angew. Chem. Int. Ed. 59 (12) (2020) 4920–4924, doi:10.1002/anie.201916529.
[36] K.W. Nam, H. Kim, Y. Beldjoudi, T.W. Kwon, D.J. Kim, J.F. Stoddart, Redox-active phenanthrenequinone triangles in aqueous rechargeable zinc batteries, J. Am. Chem. Soc. 142 (5) (2020) 2541–2548, doi:10.1021/jacs.9b12436.
[37] M.A. Khayum, M. Ghosh, V. Vijayakumar, A. Halder, M. Nurhuda, S. Kumar, M. Addicoat, S. Kurungot, R. Banerjee, Zinc ion interactions in a two-dimensional covalent organic framework based aqueous zinc ion battery, Chem. Sci. 10 (38) (2019) 8889–8894, doi:10.1039/c9sc03052b.
[38] M. Mao, C. Luo, T.P. Pollard, S. Hou, T. Gao, X. Fan, C. Cui, J. Yue, Y. Tong, G. Yang, T. Deng, M. Zhang, J. Ma, L. Suo, O. Borodin, C. Wang, A pyrazine-based polymer for fast-charge batteries, Angew. Chem. Int. Ed. 58 (49) (2019) 17820–17826, doi:10.1002/anie.201910916.
[39] H.Y. Shi, Y.J. Ye, K. Liu, Y. Song, X. Sun, A long-cycle-life self-doped polyaniline cathode for rechargeable aqueous zinc batteries, Angew. Chem. Int. Ed. 57 (50) (2018) 16359–16363, doi:10.1002/anie.201808886.
[40] J. Kumankuma-Sarpong, S. Tang, W. Guo, Y. Fu, Naphthoquinone-based composite cathodes for aqueous rechargeable zinc-ion batteries, ACS Appl. Mater. Interfaces 13 (3) (2021) 4084–4092, doi:10.1021/acsami.0c21339.
[41] H. Zhang, S. Xie, Z. Cao, D. Xu, L. Wang, H. Fang, J. Shen, M. Ye, Extended π-conjugated system in organic cathode with active C=N bonds for driving aqueous zinc-ion batteries, ACS Appl, Energy Mater, 4 (1) (2021) 655–661, doi:10.1021/acsaem.0c02526.
[42] B. Pan, J. Huang, Z. Feng, L. Zeng, M. He, L. Zhang, J.T. Vaughey, M.J. Bedzyk, P. Fenter, Z. Zhang, A.K. Burrell, C. Liao, Polyanthraquinone-based organic cathode for high-performance rechargeable magnesium-ion batteries, Adv. Energy Mater. 6 (14) (2016) 1600140, doi:10.1002/aenm.201600140.
[43] J. Wang, C.S. Chen, Y. Zhang, Hexaazatrinaphthylene-based porous organic polymers as organic cathode materials for lithium-ion batteries, ACS Sustain. Chem. Eng. 6 (2) (2017) 1772–1779, doi:10.1021/acssuschemeng.7b03165.
[44] H. Zhang, W. Sun, X. Chen, Y. Wang, Few-layered fluorinated triazine-based covalent organic nanosheets for high-performance alkali organic batteries, ACS Nano 13 (12) (2019) 14252–14261, doi:10.1021/acsnano.9b07360.
[45] Q. Wang, X. Xu, G. Yang, Y. Liu, X. Yao, An organic cathode with tailored working potential for aqueous Zn-ion batteries, Chem. Commun. 56 (79) (2020) 11859–11862, doi:10.1039/d0cc05344a.
[46] W. Wang, V.S. Kale, Z. Cao, S. Kandambeth, W. Zhang, J. Ming, P.T. Parvatkar, E. Abou-Hamad, O. Shekhah, L. Cavallo, M. Eddaoudi, H.N. Alshareef, Phenanthroline covalent organic framework electrodes for high-performance zinc-ion supercapattery, ACS Energy Lett. 5 (7) (2020) 2256–2264, doi:10.1021/acsenergylett.0c00903.
[47] F. Wan, L. Zhang, X. Wang, S. Bi, Z. Niu, J. Chen, An aqueous rechargeable zinc-organic battery with hybrid mechanism, Adv. Funct. Mater. 28 (45) (2018) 1804975, doi:10.1002/adfm.201804975.
[48] Y. Hu, Y. Gao, L. Fan, Y. Zhang, B. Wang, Z. Qin, J. Zhou, B. Lu, Electrochemical study of poly(2,6-Anthraquinonyl Sulfide) as cathode for alkali-metal-ion batteries, Adv. Energy Mater. 10 (48) (2020) 2002780, doi:10.1002/aenm.202002780.
[49] Z. Song, Y. Qian, X. Liu, T. Zhang, Y. Zhu, H. Yu, M. Otani, H. Zhou, A quinone-based oligomeric lithium salt for superior Li–organic batteries, Energy Environ. Sci. 7 (12) (2014) 4077–4086, doi:10.1039/c4ee02575j.
[50] Y. Gao, G. Li, F. Wang, J. Chu, P. Yu, B. Wang, H. Zhan, Z. Song, A high-performance aqueous rechargeable zinc battery based on organic cathode integrating quinone and pyrazine, Energy Storage Mater 40 (2021) 31–40, doi:10.1016/j.ensm.2021.05.002.
[51] S. Gu, S. Wu, L. Cao, M. Li, N. Qin, J. Zhu, Z. Wang, Y. Li, Z. Li, J. Chen, Z. Lu, Tunable redox chemistry and stability of radical intermediates in 2D covalent organic frameworks for high performance sodium ion batteries, J. Am. Chem. Soc. 141 (24) (2019) 9623–9628, doi:10.1021/jacs.9b03467.
[52] Y. Liu, H. Dai, L. Wu, W. Zhou, L. He, W. Wang, W. Yan, Q. Huang, L. Fu, Y. Wu, A large scalable and low-cost sulfur/nitrogen dual-doped hard carbon as the negative electrode material for high-performance potassium-ion batteries, Adv. Energy Mater. 9 (34) (2019) 1901379, doi:10.1002/aenm.201901379.
[53] Z. Ye, S. Xie, Z. Cao, L. Wang, D. Xu, H. Zhang, J. Matz, P. Dong, H. Fang, J. Shen, M. Ye, High-rate aqueous zinc-organic battery achieved by lowering HOMO/LUMO of organic cathode, Energy Storage Mater. 37 (2021) 378–386, doi:10.1016/j.ensm.2021.02.022.
[54] S. Zheng, L. Miao, T. Sun, L. Li, T. Ma, J. Bao, Z. Tao, J. Chen, An extended carbonyl-rich conjugated polymer cathode for high-capacity lithium-ion batteries, J. Mater. Chem. A 9 (5) (2021) 2700–2705, doi:10.1039/d0ta11648c.
[55] V. Augustyn, P. Simon, B. Dunn, Pseudocapacitive oxide materials for high-rate electrochemical energy storage, Energy Environ. Sci. 7 (5) (2014), doi:10.1039/c3ee44164d.
[56] D. Chao, C. Zhu, P. Yang, X. Xia, J. Liu, J. Wang, X. Fan, S.V. Savilov, J. Lin, H.J. Fan, Z.X. Shen, Array of nanosheets render ultrafast and high-capacity Na-ion storage by tunable pseudocapacitance, Nat. Commun. 7 (2016) 12122, doi:10.1038/ncomms12122.
[57] C. Chen, Y. Wen, X. Hu, X. Ji, M. Yan, L. Mai, P. Hu, B. Shan, Y. Huang, Na(+) intercalation pseudocapacitance in graphene-coupled titanium oxide enabling ultra-fast sodium storage and long-term cycling, Nat. Commun. 6 (2015) 6929, doi:10.1038/ncomms7929.
[58] Z. Ouyang, D. Tranca, Y. Zhao, Z. Chen, X. Fu, J. Zhu, G. Zhai, C. Ke, E. Kymakis, X. Zhuang, Quinone-enriched conjugated microporous polymer as an organic cathode for Li-ion batteries, ACS Appl. Mater. Interfaces 13 (7) (2021) 9064–9073, doi:10.1021/acsami.1c00867.
[59] T. Cai, Y. Han, Q. Lan, F. Wang, J. Chu, H. Zhan, Z. Song, Stable cycling of small molecular organic electrode materials enabled by high concentration electrolytes, Energy Storage Mater. 31 (2020) 318–327, doi:10.1016/j.ensm.2020.06.032.
[60] G. Zhang, Y. Yang, T. Zhang, D. Xu, Z. Lei, C. Wang, G. Liu, Y. Deng, FeIII chelated organic anode with ultrahigh rate performance and ultra-long cycling stability for lithium-ion batteries, Energy Storage Mater. 24 (2020) 432–438, doi:10.1016/j.ensm.2019.07.018.